ChemPubSoc Europe

DOI: 10.1002/chem.201606029

CHEMISTRY A European Journal Full Paper

Magnetic Properties | *Hot Paper*

Dynamic Magnetic and Optical Insight into a High Performance Pentagonal Bipyramidal Dy^{III} Single-Ion Magnet

Yan-Cong Chen,[a] Jun-Liang Liu,*[a] Yanhua Lan,[b] Zhi-Qiang Zhong,[c] Akseli Mansikkamäki,[d, e] Liviu Ungur,[d, f] Quan-Wen Li,[a] Jian-Hua Jia,[a] Liviu F. Chibotaru,[d] Jun-Bo Han,[c] Wolfgang Wernsdorfer,[b] Xiao-Ming Chen,[a] and Ming-Liang Tong*[a]

Abstract: The pentagonal bipyramidal single-ion magnets (SIMs) are among the most attractive prototypes of high-performance single-molecule magnets (SMMs). Here, a fluorescence-active phosphine oxide ligand $CyPh_2PO$ (=cyclohexyl-(diphenyl)phosphine oxide) was introduced into $[Dy(CyPh_2PO)_2(H_2O)_5]Br_3{\cdot}2(CyPh_2PO){\cdot}EtOH{\cdot}3H_2O$, and combined dynamic magnetic measurement, optical characterization, ab initio calculation, and magneto-optical correlation of this high-performance pseudo-D_{5h} Dy^{III} SIM with large U_{eff} (508(2) K) and high magnetic hysteresis temperature (19 K) were performed. This work provides a deeper insight into the rational design of promising molecular magnets.

Introduction

Single-molecule magnets (SMMs) have attracted strong interest in recent years, as they can be trapped in one of the bistable magnetic states that are separated by an energy barrier. Among the most promising candidates for high-density information storage, quantum processing, and spintronics,[1] a good SMM should combine a large energy barrier, high blocking temperature, and weak quantum tunneling of magnetization (QTM). The early cases of polymetallic clusters of transition metals showed highly suppressed QTM,[2] but increasing the energy barrier hit a bottleneck due to the difficulty of combining the large spin states and high anisotropies together. Lanthanide metal ions, especially Tb^{III}, Dy^{III}, Ho^{III}, and Er^{III} with intrinsic large spin-orbit interactions,[3] have been extensively studied recently for SMMs, and the radical-bridged dilanthanide complexes achieved high blocking temperatures up to 14 K.[4] For most of the high performance monometallic lanthanide SMMs, a smart strategy is to stabilize some typical coordination symmetries for reducing the off-diagonal elements of orbit-lattice interaction matrix, and therefore suppressing QTM.[3b,e,5] Based on crystal-field theory,[6] besides square antiprismatic complexes toward D_{4d} symmetry[3b,5e,f,7] and linear 2-coordinated[5a–c] complexes/sandwich-type complexes toward $D_{\infty h}$ symmetry,[3d,8] pentagonal bipyramidal complexes are on the way to getting close to the D_{5h} symmetry that suppresses quantum tunneling and exhibits record anisotropic barriers. These facts illustrate that pseudo-D_{5h}-symmetry single ion magnets (SIMs) are highly attractive, and it is worth understanding the magnetic dynamics and energy structures.[9] Although strict five-fold symmetry is forbidden in conventional crystals, researchers have been trying to push the local symmetry to the limit.[9,10]

Recently, we investigated the pentagonal bipyramidal Dy^{III} SIMs, which comprise a highly symmetrical $[Dy(Cy_3PO)_2(H_2O)_5]^{3+}$ (Cy_3PO=tricyclohexyl phosphine oxide) core.[9c] The strong axial crystal field provided by the phosphine oxide, combined with the weak equatorial ligands arranged in pseudo-5-fold symmetry, led to energy barriers around 500 K and a record-breaking magnetic hysteresis temperature up to

[a] *Y.-C. Chen, Dr. J.-L. Liu, Q.-W. Li, Dr. J.-H. Jia, Prof. Dr. X.-M. Chen, Prof. Dr. M.-L. Tong*
Key Laboratory of Bioinorganic and Synthetic Chemistry of Ministry of Education, School of Chemistry and Chemical Engineering
Sun Yat-Sen University, Guangzhou 510275 (P. R. China)
E-mail: liujliang5@mail.sysu.edu.cn
tongml@mail.sysu.edu.cn

[b] *Dr. Y. Lan, Prof. Dr. W. Wernsdorfer*
Institut Néel
CNRS & Université Joseph Fournier, BP 166
25 rue des Martyrs
38042 Grenoble Cedex 9 (France)

[c] *Z.-Q. Zhong, Prof. Dr. J.-B. Han*
Wuhan National High Magnetic Center
Huazhong University of Science and Technology
Wuhan 430074 (P. R. China)

[d] *A. Mansikkamäki, Dr. L. Ungur, Prof. Dr. L. F. Chibotaru*
Theory of Nanomaterials Group, and
INPAC-Institute of Nanoscale Physics and Chemistry
Katholieke Universiteit Leuven
Celestijnenlaan 200F
3001 Leuven (Belgium)

[e] *A. Mansikkamäki*
Department of Chemistry, Nanoscience Center
University of Jyväskylä
P. O. Box 35, 40014 Jyväskylä (Finland)

[f] *Dr. L. Ungur*
Theoretical Chemistry Group
Department of Chemistry
Lund University
Getingevagen 60
22201, Lund (Sweden)

Supporting information and the ORCID identification number(s) for the author(s) of this article can be found under http://dx.doi.org/10.1002/chem.201606029.

20 K for the Br derivative. To the best of our knowledge, it is also the first report on Ln-SIMs based on phosphine oxide, which is undoubtedly an emerging and promising family in this area and requires deeper understanding on their multifaceted behaviors and magneto-structural correlations.

Based on the previous study, aromatic substituent groups were introduced into the system as sensitive antennas to promote the luminescence of Dy^{III} ions. The fluorescence spectra of rare earth ions can provide extremely valuable information on the energy levels, which is a direct probe and also a solid support to the magnetic studies and ab initio calculations. The title complex, $[Dy(CyPh_2PO)_2(H_2O)_5]Br_3{\cdot}2\,(CyPh_2PO){\cdot}EtOH{\cdot}3\,H_2O$ (**1**, $CyPh_2PO$ = cyclohexyl(diphenyl)phosphine oxide), comprises a $[Dy(R_3PO)_2(H_2O)_5]^{3+}$ analogue core that retains the SMM properties. In addition, the advantages of **1** compared with its predecessor include: 1) a further increased symmetry by a C_2 axis through the Dy^{III} ion; 2) the feasibility to obtain suitable single crystals for micro-SQUID measurement; 3) the introduction of aromatic substituent groups to yield prominent fluorescence spectra for luminescence studies. From a comprehensive study of crystallography, dc/ac magnetic characterization, single-crystal micro-SQUID measurement, and luminescence spectroscopy, a deeper understanding of the magneto-structural correlation, the relaxation dynamics, and the QTM mechanism of SMMs was reached. These combined with the state-of-the-art ab initio calculations shall shed light into the further study on SMMs.

Results and Discussion

Crystal structure

The title compound can be synthesized from $DyBr_3$ and $CyPh_2PO$ in a H_2O/EtOH mixed solution, followed by recrystallization in EtOH and slow evaporation in ambient conditions (see the Experimental Section for details). Single-crystal diffraction shows that **1** crystallizes in the orthorhombic space group $C222_1$ and each asymmetric unit contains one Dy^{3+} ion, two coordinated $CyPh_2PO$ ligands (oriented in opposite directions), five coordinated waters in the equatorial plane, two free ligands, three Br^- ions in the outer coordination spheres, and two EtOH molecules (Figure 1 a). An additional symmetry of a C_2 axis (compared with the Cy_3PO analogue) through the Dy1–O1W provides the crystallographic guarantee of equal bond lengths and angles for the main anisotropy axis along O1-Dy-O1A, which can be regarded as a step further toward the ideal pentagonal bipyramid geometry. The value of continuous shape measures calculations (CShM) is 0.174, which is only slightly larger than the most perfect pseudo-D_{5h} symmetry Ln-SIM reported to date ($[Dy(Cy_3PO)_2(H_2O)_5]Br_3{\cdot}2\,(Cy_3PO){\cdot}2\,H_2O{\cdot}2\,EtOH$, CShM = 0.142, Table S2 in the Supporting Information).[9c] Nevertheless, the actual symmetry for **1** is C_2.

For the outer coordination sphere, a five-pointed star is formed by hydrogen bonds between the five coordinated H_2O molecules, three Br^- ions, and two free ligands (Figure 1 b), which helps the stabilization of the pseudo-D_{5h} symmetry of the first coordination sphere. Overall, the local environment of

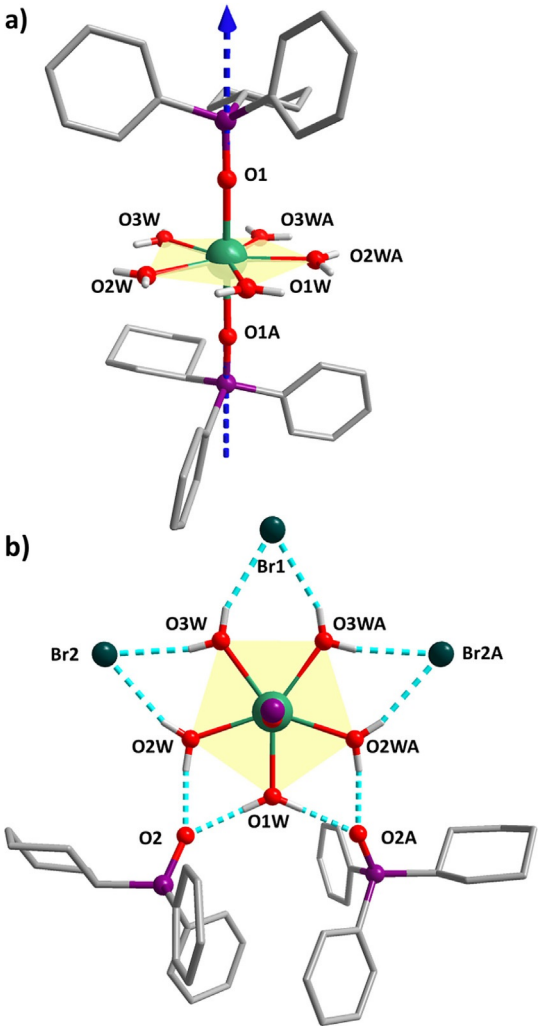

Figure 1. Crystal Structures of **1** emphasizing the pseudo-five-fold symmetry. a) Coordination environment of Dy^{III} in **1**. The blue dashed line represents the orientation of the main magnetic axes of the lowest Kramers doublets. b) Outer coordination sphere connected with hydrogen bonds in **1**. H atoms of $CyPh_2PO$ are omitted for clarity. Color Codes: Dy, green; P, purple; Br, cyan; O, red; C, gray; H, light gray. Symmetry code (A): $1-x, y, 0.5-z$.

Dy^{3+} in **1** is a highly compressed pentagonal bipyramid with average Dy–O distances of 2.217 (axial) and 2.364 Å (equatorial). Face-to-face and edge-to-face π–π stacking is formed between the benzyl rings of the coordinated ligands and the uncoordinated ones. Between the discrete molecules, the nearest Dy–Dy distance in the crystal structure is as far as 13.8 Å and there are no direct or super-exchange interactions through chemical bonds.

Magnetic characterization

Variable-temperature magnetic susceptibilities were measured on polycrystalline samples of **1** under a 0.1 T dc field (Figure 2 a). At room temperature the $\chi_M T$ value is 13.9 $cm^3\,K\,mol^{-1}$; a little lower than the expected value for a free Dy^{3+} ion (14.17 $cm^3\,K\,mol^{-1}$). Upon cooling, $\chi_M T$ gradually decreases and then suddenly drops below approximately 12 K. The zero-field-

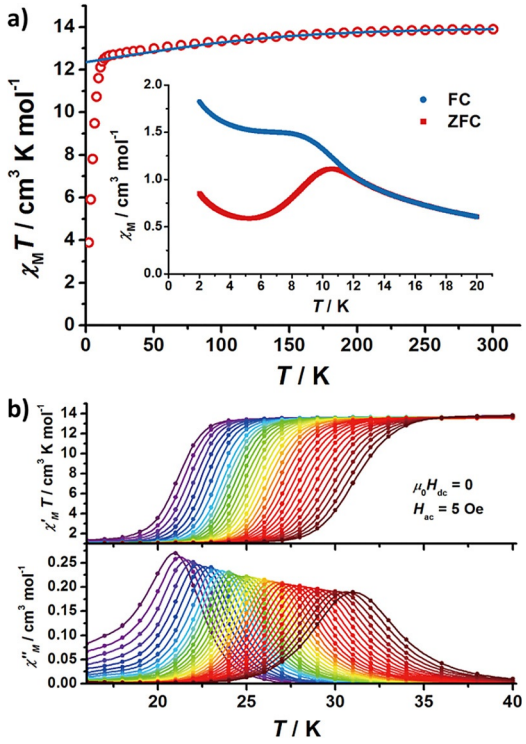

Figure 2. a) Temperature dependence of the molar magnetic susceptibility $\chi_M T$ products and the zero-field-cooled/field-cooled (ZFC-FC) magnetic susceptibilities (inset) for **1** under a 0.1 T dc field sweeping at 2 K min^{-1} in warming mode. The solid line corresponds to the ab initio calculations. b) Temperature dependence of the in-phase $\chi'_M T$ product and out-of-phase χ''_M for **1** in zero dc field with an ac frequency of 1–1488 Hz.

cooled/field-cooled (ZFC-FC) magnetization under a 0.1 T in warm mode (2 K min^{-1}) (inset of Figure 2a) shows a clear divergence below 11 K with a peak at 10.5 K, indicating the process into magnetic blocking. The magnetization values approaching 5 $N\beta$ and the overlapped M versus H/T curves (Figure S5 in the Supporting Information) provide evidence of far-separated excited doublets for Dy^{3+}.

To reveal the dynamic magnetic behaviors, variable-temperature and variable-frequency ac magnetic susceptibilities were measured in zero dc field and a 0.1 T dc field. From the temperature-dependent data (Figure 2b), the patterns are quite typical for SMMs, with the 1488 Hz peak located at 31 K down to the 1 Hz peak located at 21 K. No overwhelming QTM can be observed on the ac data in the measured window.

For the frequency-dependent measurement (Figure 3), the low-frequency limit was pushed to 0.1 Hz and the ac peaks still keep shifting towards the low frequency region. Moreover, the ac susceptibilities are almost unaffected by the application of a 0.1 T dc field (Figure 3b). For the high temperature region, the temperature dependence of the relaxation time τ perfectly obeys the Arrhenius law, corresponding to the Orbach process, and the best fit gives $U_{eff} = 508(2)$ K, $\tau_0 = 8.6 \times 10^{-12}$ s for zero dc field and $U_{eff} = 503(4)$ K, $\tau_0 = 9.5 \times 10^{-12}$ s for a 0.1 T dc field (Figure 4a).

To investigate the slow relaxation behavior at lower temperatures, the measured relaxation time was extended using dc

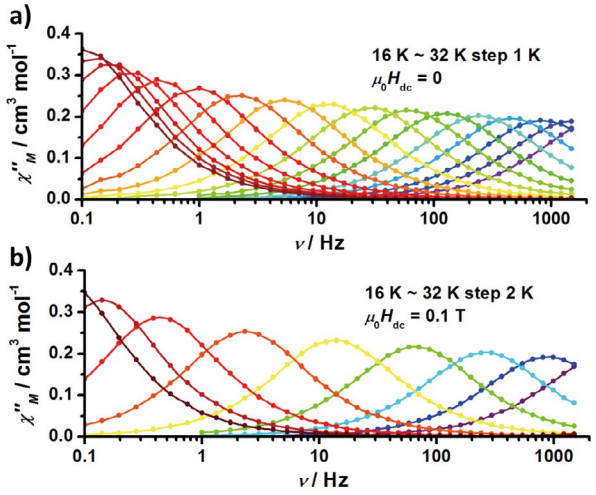

Figure 3. Frequency dependence of the out-of-phase χ''_M in a) zero dc field and b) 0.1 T dc field for **1**. Lines are guides for the eyes.

magnetization decay. The relaxation dynamics can be fitted with the multiple relaxation equation [Eq. (1)]:

$$\tau^{-1} = \tau_0^{-1}\exp(-U_{eff}/k_B T) + CT^n + \tau_{QTM}^{-1} \quad (1)$$

involving an Arrhenius term for the Orbach process, a power

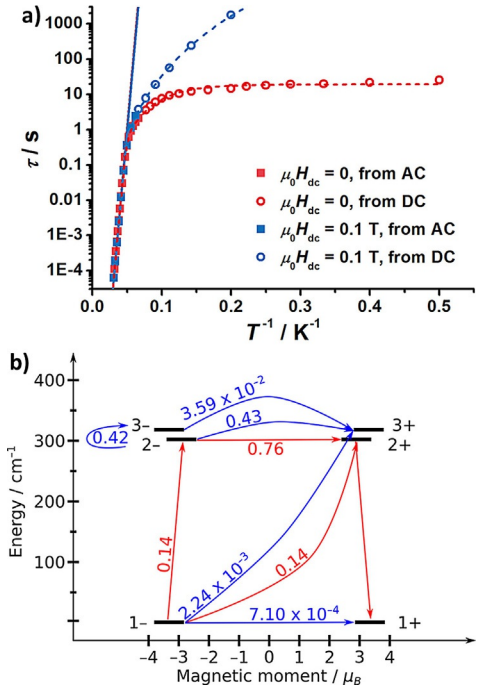

Figure 4. a) Temperature dependence of the relaxation time τ in zero dc field (red) and a 0.1 T dc field (blue) for **1**. The solid lines are the best fits to the Arrhenius law, whereas the dashed lines are the best fit to the multiple relaxation equation. b) Magnetization blocking barrier of **1**. The lowest spin-orbit states are arranged according to the magnitude of their magnetic moments on the horizontal axis. The numbers next to arrows connecting two states display the average transition magnetic moment matrix element between the respective states. The most probable relaxation route is indicated by red arrows and takes place via the first excited Kramers doublet.

function term for the Raman process with $n = 4.0(2)$ and slowly goes to a platform with $\tau_{QTM} = 19.5(8)$ s for zero dc field. When the final dc field is set as 0.1 T, the relaxation times keeps rising with $n = 5.61(4)$ and goes up to 1775 s at 5 K, showing the suppression of QTM (Figure 4a).

Magnetic hysteresis loops can be observed as the extremely slow magnetic relaxation rate at low temperatures, even on a conventional PPMS-VSM (Figure 5). The butterfly shape is typical, due to the faster relaxation around zero field, and the major reasons are the unsuppressed QTM from: 1) the deviation of the symmetry; 2) the hyperfine interaction, and 3) the dipolar interactions. The hysteresis loops become narrower with the increase of temperature, and the remanent magnetization (M_r) and coercive field (H_c) also become smaller (Figure S7 in the Supporting Information). The hysteresis temperature is conservatively considered to be 19 K with the field ramping speed of 0.02 Ts^{-1} (at higher temperatures the measurement falls inside instrumental error when $H_c < 0.01$ T), which is comparable with the Cy_3PO derivative[9c] and higher than that of [Dy(bbpen)Br] (H_2bbpen = N,N′-bis(2-hydroxybenzyl)-N,N′-bis(2-methylpyridyl)ethylenediamine).[9d] It should be noted that the hysteresis temperature is usually different from the peak temperature of ZFC susceptibilities. Indeed, there will not be a strict definition of blocking temperatures for SMMs; it depends on different measurements, as the slow relaxation of magnetization is not a real "blocking" like that in phase-changing materials. In addition, some of the extremely high energy barriers do not guarantee the proportional increase of the relaxation times,[9d,10b,c] as the relaxation is already dominated by a Raman process in the lower temperature region.

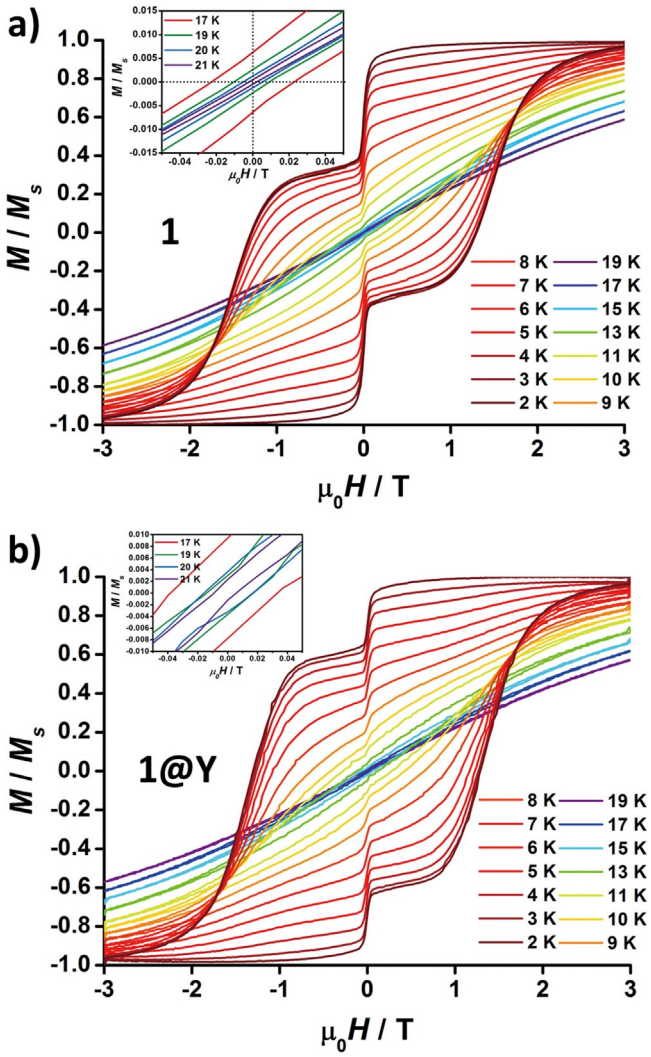

Figure 5. Normalized magnetic hysteresis loops for a) **1** and b) **1@Y**. The data were continuously collected at intervals of 1 s with the field ramping speed of 0.02 Ts^{-1} at various temperatures.

Further study of the diluted sample **1@Y** does not show much difference from **1**. Fitting the ac susceptibilities yields the consistent $U_{eff} = 467(5)$ K, $\tau_0 = 2.4 \times 10^{-11}$ s for zero dc field and $U_{eff} = 465(5)$ K, $\tau_0 = 2.4 \times 10^{-11}$ s for a 0.1 T dc field (Figures S9–S11 in the Supporting Information). The divergence of ZFC-FC curves is also observed below 11 K with a peak at 10.5 K (Figure S12). The remanent magnetization (M_r) becomes larger after the dilution (Figure 5b), which was attributed to the weakening of intermetallic magnetic interactions, though the magnetic hysteresis loops still remain open up to 19 K.

Micro-SQUID measurement

To extend the characterization down to ultra-low temperatures, micro-SQUID measurements were performed on a single crystal of **1**. The hysteresis loops at 4 K show similar shapes to the powder sample (Figure 6a), which become even more prominent at 0.03 K (Figure 6b). For the decay of the dc magnetization at zero applied field, the single-crystal measurements should be comparable to the powder measurements and the relaxation time obtained from these two measurements should be converged in the same temperature regime. As illustrated in the plots (Figure 6d), although the two datasets follow in the same trend, they could be converged only with a multiplying factor of 1.7. Such a difference could be due to the fact that there is no way to set the field exactly as zero in conventional SQUID and the remanent field always exists.

Luminescence study

The introduction of aromatic substituent groups in **1** leads to good fluorescence spectra both at room temperature and at low temperature, which provides valuable information on the energy levels. In general, the emission spectrum of **1** (Figure S13 in the Supporting Information) shows the characteristic peaks for Dy^{III} with three groups of sharp peaks, corresponding to the f–f transition, at around 475 nm (21 000 cm^{-1}, $^4F_{9/2} \rightarrow {}^6H_{15/2}$), 575 nm (17 400 cm^{-1}, $^4F_{9/2} \rightarrow {}^6H_{13/2}$), and 670 nm (15 000 cm^{-1} $^4F_{9/2} \rightarrow {}^6H_{11/2}$). Here, the $^4F_{9/2} \leftrightarrow {}^6H_{15/2}$ transitions around 21 000 cm^{-1} are focused on, that is, those involving the lowest-lying energy levels that are crucial to the magnetic dynamics (Figure 7).

At room temperature, the multiple peaks are difficult to distinguish. On lowering the temperature, the $^6H_{15/2} \rightarrow {}^4F_{9/2}$ absorption and the $^6H_{15/2} \rightarrow {}^4F_{9/2} \rightarrow {}^6H_{13/2}$ excitation spectra become sharper, and the peaks at 20 983 cm^{-1} (labelled 2 in Fig. 7a)

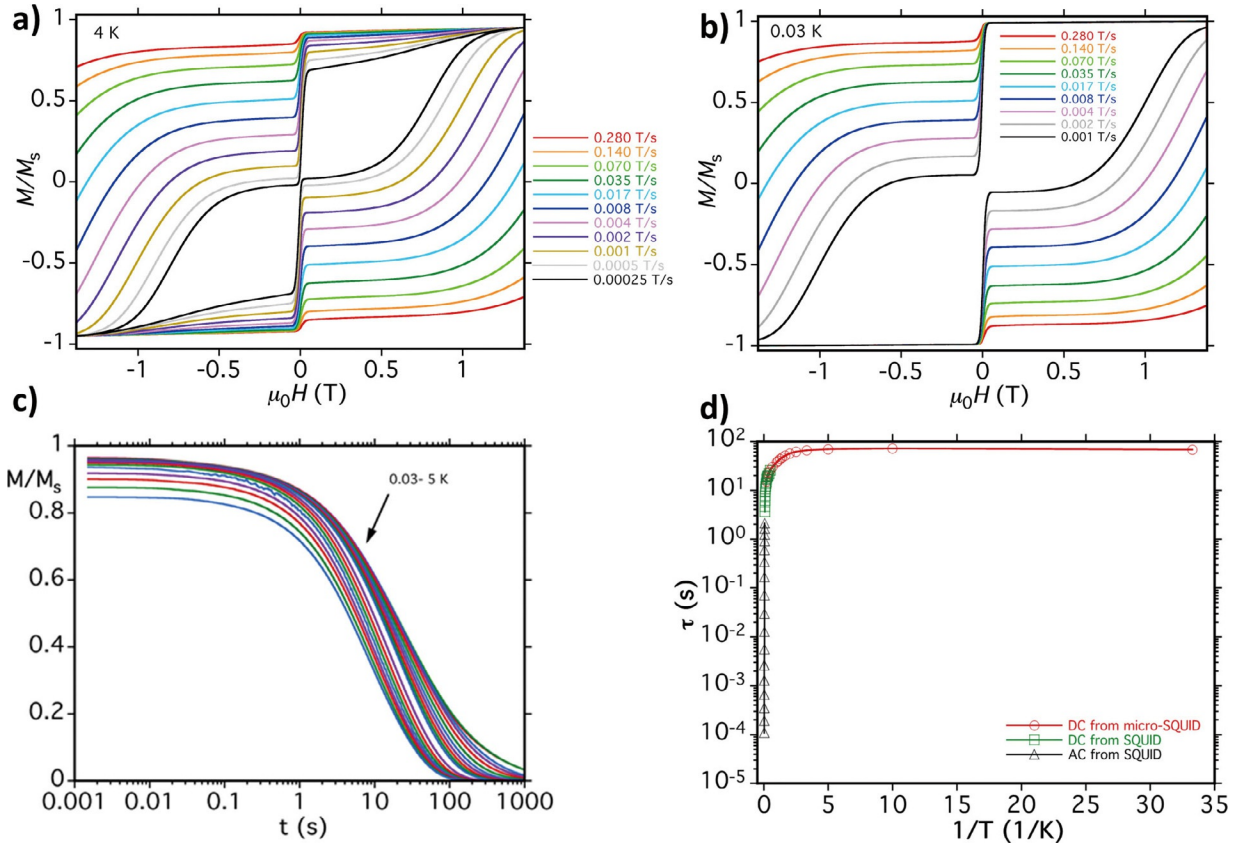

Figure 6. Dynamic magnetic properties for **1** measured on micro-SQUID: a) Normalized magnetic hysteresis loops at 4 K; b) normalized magnetic hysteresis loops at 0.03 K; c) the decay of the normalized dc magnetization at various temperatures; d) temperature dependence of the relaxation time τ compared with the ac (black) and dc (green) data from SQUID.

and 20914 cm^{-1} (labelled 3) disappear, indicating the depopulation of excited states. At 10 K, the last peak of the absorption and excitation spectra overlap perfectly with the first peak of the emission spectra at 21308 cm^{-1} (labelled 1), which is assigned as the ground-to-ground transition of $^4F_{9/2} \leftrightarrow {}^6H_{15/2}$ (red arrow in Figure 7b). Then, the eight Kramers doublets from the splitting of the $^6H_{15/2}$ multiplet can be successively determined from the fine structure of the $^4F_{9/2} \rightarrow {}^6H_{15/2}$ emission. The huge intensity difference of the emission peaks is also believed to correspond to the extent of mixing of the wave functions, as these transitions are intrinsically forbidden, whereas the selection rules can be broken by lanthanide-crystal field interactions.

Photoluminescence measurements were also performed under a pulsed high magnetic field up to 37 T to probe the magnetic response.[12] Although several weak peaks cannot be observed, the pulse-field emission still matches well with the conventional spectra. Significant effect of the Zeeman splitting is observed with the general shift towards lower wavenumber (owing to the ground-doublet splitting of the $^4F_{9/2}$ state) and the further splitting into pairs of peaks within the $^6H_{15/2}$ state. The asymmetric character around 20900 cm^{-1} might indicate the overlapping of multiple peaks with different center positions and Zeeman splitting, which is in agreement with the close lying of the first and second excited state (labelled 2 and 3 in Figure 7a). Also, the small splitting of the strongest peak at 20914 cm^{-1} (labelled 3) rules out the possibility to involve the ground doublet, which has the largest g_z (see calculation for details). Here, the energy gaps from the ground doublet to these two excited doublets are 322 and 396 cm^{-1}, respectively, matching well with the spin-reversal barrier of 353 cm^{-1} for **1** and 324 cm^{-1} for **1@Y** determined by the magnetic measurements.

Ab initio calculations

Further insight into the electronic structure and magnetic properties of **1** was obtained by quantum chemistry calculations. The geometry of **1** was extracted from the crystal structure and the positions of hydrogen atoms were optimized at the DFT level. This was done because the coordinates of the hydrogen atoms refined from the diffraction data are usually not very accurate and the hydrogens of the coordinated water molecules lie close to the Dy ion and may therefore have an appreciable effect on the crystal field. The optimization retains the nearly planar pseudo-D_{5h} arrangement of the five water molecules. The structure used in the DFT and ab initio calculations included, in addition to the complex **1**, the outer coordination sphere containing the three bromide ions and the two free ligands hydrogen-bonded to the coordinated water molecules (Figure 1). Calculations were also conducted on various truncated structures but the results show that any simplifica-

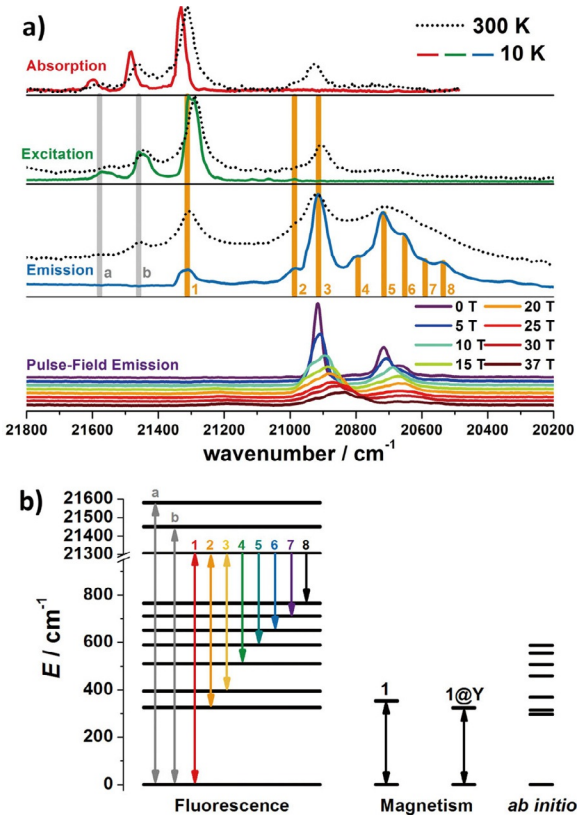

Figure 7. a) Fluorescence spectra of **1** showing the $^4F_{9/2} \leftrightarrow {}^6H_{15/2}$ peaks. The absorption, excitation ($\lambda_{em} = 574$ nm), and emission ($\lambda_{ex} = 361$ nm) spectra were measured at 300 K (black dotted lines) and 10 K (color solid lines), and the pulse-field emission spectra were measured at 5 K. Vertical lines indicate the optical transitions between the microstates of $^4F_{9/2}$ and $^6H_{15/2}$ and the emission spectra are plotted in logarithmic intensity for clarity. b) Energy levels determined by the fluorescence spectra of **1** compared with the magnetic blocking barrier and ab initio calculation results. Note the higher energy transitions (grey arrows) involve the excited states of the $^4F_{9/2}$ state.

tion of the structure leads to qualitative changes in the energy spectrum and the magnetic properties.

The calculated *g*-tensors of the eight lowest Kramers doublets are listed in Table 1. The ground doublet is highly axial ($g_x = 0.0002$, $g_y = 0.0002$, $g_z = 19.8812$) explaining the prominent SMM behavior of **1** at low temperatures. The orientations of the main anisotropy axis (g_z) of the ground Kramers doublet is illustrated in Figure 1a, and is aligned roughly along the main rotational axis of the pseudo-D_{5h} symmetry around the Dy ion and deviates from the two axial Dy–O bond vectors by an angle of 2.9°. The main axis of the first excited Kramers doublet lies along the C_2 axis of the crystal structure and is near perfectly perpendicular to the ground axis with an angle of 90.0° between them. The third axis lies again almost parallel to the main rotational axis with an angle of 0.3° between it and the ground axis.

To elucidate the effects of the electronic structure on the relaxation of magnetization in **1** the magnetization blocking barrier was also studied using a previously proposed methodology.[13a] The results are summarized in Figure 4b and show that the most probable relaxation pathway takes place via the first excited Kramers doublet. The local pseudo-D_{5h} symmetry

Table 1. Calculated *g*-tensors of the eight lowest Kramers doublets arising from the crystal field splitting of the $^6H_{15/2}$ manifold

KD	g_x	g_y	g_z
1	0.0002	0.0002	19.8812
2	0.9571	3.4268	16.6964
3	0.0881	0.1268	16.9229
4	3.3031	4.5458	8.7070
5	1.4008	3.7771	6.5247
6	0.2470	0.3874	13.6266
7	0.2963	1.2140	11.2279
8	0.5039	1.0113	13.1702

around the Dy ion leads to suppression of the QTM process indicated by the relatively small value of the matrix element connecting the two components of the ground doublet. The lower symmetry introduced by the outer coordination sphere leads to rotation of the main magnetic axis of the first excited doublet into an orientation parallel to the true C_2 axis of the crystal structure, which lies perpendicular to the ground axis. As previously demonstrated, the large angle between the two Kramers doublets leads to large transverse magnetic matrix elements between the components of the respective doublets.[13b] This allows the magnetization to traverse through the barrier and leads to lowering of the blocking barrier compared to an analogous complex in ideal D_{5h} symmetry.

Although the properties of Kramers doublets—such as the *g*-tensors and transition magnetic moments—are well reproduced at CASSCF (complete active space self-consistent field) level, quantitative comparison of the calculated energy levels with those obtained from the luminescence spectrum require explicit treatment of dynamic correlation. This can be achieved by applying a second-order correction to the CASSCF energies using the extended multistate (XMS) CASPT2 method.[13c] Treatment of the full molecular structure, including the outer coordination sphere, is not feasible at this level in terms of computational costs, whereas simplification of the structure may result into qualitative differences in the calculated energetics. Thus, dynamic correlation effects were treated as a correction to the ab initio crystal field potential of the $^6H_{15/2}$ ground multiplet (see the Supporting Information for a detailed description of the procedure) and a corrected crystal-field Hamiltonian was diagonalized to obtain the final spectrum. The crystal-field corrected energies of the eight lowest Kramers doublets are presented in Table S4 (see the Supporting Information) along with the respective values calculated at CASSCF level for the full geometry and at CASSCF and XMS-CASPT2 levels for a truncated geometry where the phenyl and cyclohexyl groups of the ligands have been replaced with methyl groups. The results clearly show that dynamic correlation and the full structure are required to approach the experimental levels.

The energy of the first excited Kramers doublet calculated using the crystal-field correction approach is 297 cm^{-1}, which is in good agreement with the energy difference of 322 cm^{-1} obtained from the luminescence spectrum. The value is also in semi-quantitative agreement with the experimental barrier heights 353 cm^{-1} for **1** and 324 cm^{-1} for **1@Y** from magnet-

ism. Agreement with the higher excited states is poorer. This deviation most likely results from the approximate nature of the crystal-field correction procedure employed in this study. Enlarging the active space of the CASSCF method by explicitly correlating several ligand-type orbitals and/or metal's occupied and virtual orbitals is expected increase the quality of the reference wave function, leading to an even closer agreement for the excited states. This was recently demonstrated for an Er-trensal complex (H_3trensal = 2,2′,2″-tris(salicylideneimido)trimethylamine),[14] for which a larger active space increased the overall agreement for each of the crystal-field levels of the ground $J = 15/2$ multiplet, as well as for their properties.

Conclusion

In conclusion, while preserving the large energy barrier and high hysteresis temperature, single-crystal micro-SQUID measurements were successfully performed at ultra-low temperature and the characteristic lanthanide photoluminescence was introduced into the family of pentagonal bipyramidal Dy^{III} single-ion magnets based on phosphine oxide. The ac, dc, and micro-SQUID relaxation data follow in the same trend and the hysteresis loops become wider when going down to 0.04 K. The fluorescence spectra provide crucial information on the energy levels that correspond well with the magnetic measurements and show semi-quantitative agreement with the ab initio calculations. It should be pointed out that the magnetic blocking in many of these SMMs with high energy barriers is controlled by the Raman process rather than the Orbach process, which requires deeper understanding in the future. Additionally, the fast QTM around zero field sets up a limit for the further increase of the relaxation time. Efforts regarding this could be focused on the fine-tuning of the magnetic interactions and exploration of the lanthanide nuclides of suitable nuclear spins in a SIM/SMM system.

Experimental Section

General procedures

All reagents were commercially available and used as received without further purification. The elemental analyses were performed with an Elementar Vario-EL CHN elemental analyzer. The IR spectra were recorded using a Thermo Nicolet AVATAR 330 FT-IR spectrometer. The powder XRD patterns were recorded on a Bruker D8 X-Ray diffractometer with $Cu_{K\alpha}$ radiation. Thermogravimetric analysis (TGA) was carried out on a NETZSCH TG209F3 thermogravimetric analyzer. The ICP-AES analyses were performed with a TJA IRIS (HR) spectrometer.

Synthesis

$[Dy(CyPh_2PO)_2(H_2O)_5]Br_3 \cdot 2(CyPh_2PO) \cdot EtOH \cdot 3H_2O$ (**1**) was synthesized by dissolving hydrated $DyBr_3$ (0.2 mmol) and $CyPh_2PO$ (0.4 mmol) in a H_2O/EtOH (1:9, 4 mL) mixed solution, followed by slow evaporation, under ambient conditions, to almost dryness. Then EtOH (2 mL) was added for recrystallization. Colorless crystals suitable for X-ray analysis began to grow after 3 days, which were then collected by filtration, washed with cold EtOH and then dried in air (yield ca. 40%). The disordered solvent molecules in the voids were unable to be determined by single-crystal diffraction but confirmed through elemental analysis and thermogravimetric analysis. Elemental analysis (calcd, found) for $C_{76}H_{112}P_4Br_3DyO_{14}$ (**1**): C (51.40, 51.47), H (6.35, 6.02); IR: $\tilde{\nu} = 3275$(br), 2933(s), 2852(s), 1632(m), 1485(m), 1439(s), 1176(s), 1135(s), 1120(s), 1095(s), 999(m), 887(m), 746(s), 725(s), 700(s), 557(s), 536(s) cm^{-1}; The diluted sample **1@Y** was synthesized in the same way but with $DyBr_3$:$YBr_3 = 1:19$. The dilution ratios were confirmed by both the magnetization (ca. 4%) and ICP-AES analyses (5 ± 0.5%), and the phase purity was checked by powder XRD; elemental analysis (calcd, found) for $C_{76}H_{112}P_4Br_3Y_{0.95}Dy_{0.05}O_{14}$ (**1@Y**): C (53.51, 53.61), H (6.62, 6.21); IR: $\tilde{\nu} = 3256$(br), 2933(s), 2852(s), 1633(m), 1487(m), 1439(s), 1144(s), 1121(s), 1092(s), 999(m), 889(m), 825(m), 747(s), 727(s), 698(s), 557(s), 534(s) cm^{-1}.

X-ray crystallography

Single-crystal diffraction data was recorded at 150(2) K on a Rigaku R-AXIS SPIDER Image Plate diffractometer with $Mo_{K\alpha}$ radiation, solved by direct methods, and refined using the SHELXTL program.[15] Crystal data and structure refinement are listed in the Supporting Information, Tables S1–S3. CCDC 1519258 and 1519259 contain the supplementary crystallographic data for this paper. These data are provided free of charge by The Cambridge Crystallographic Data Centre.

Magnetic measurements

The dc and ac magnetic measurements were performed on the polycrystalline samples using a Quantum Design MPMS XL-7 SQUID magnetometer. The ZFC-FC (0.1 T, 2 K min^{-1}), hysteresis (0.02 T s^{-1}), and relaxation were measured on a Quantum Design PPMS with VSM option. The single-crystal measurements down to ultra-low temperature were performed on a micro-SQUID.[16] Diamagnetic correction was performed based on Pascal's coefficients. In the lower temperature region, the relaxation rate was determined by measuring the dc magnetization decay after the removal of a saturated field of 3 T.

Optical measurements

The luminescence spectra were recorded on an Edinburgh FLS-980 Fluorescence spectrometer equipped with Xenon light, PMT detector, and ALS cryostat down to 10 K. The slit and step were set to 0.1 nm to capture the detailed splitting of the peaks. The pulsed high magnetic field photoluminescence measurement was performed at Wuhan National High Magnetic Center with a laser-fiber spectrometer setup operating at 5 K. The magnitude of magnetic field is detected at the falling side of a magnetic pulse and each luminescence spectrum was captured within 1 ms.

Acknowledgements

This work was supported by the "973 Project" (2014CB845602), the NSFC (Grant No.s 21620102002, 21371183, and 91422302), and the NSF of Guangdong (S2013020013002).

Conflict of interest

The authors declare no conflict of interest.

Keywords: dysprosium · fluorescence · lanthanide · magnetic properties · single-molecule magnets

[1] a) D. Gatteschi, R. Sessoli, J. Villain, *Molecular Nanomagnets*, Oxford University Press, Oxford, **2006**; b) M. N. Leuenberger, D. Loss, *Nature* **2001**, *410*, 789 – 793; c) W. Wernsdorfer, *Science* **1999**, *284*, 133 – 135; d) L. Bogani, W. Wernsdorfer, *Nat. Mater.* **2008**, *7*, 179 – 186; e) M. Mannini, F. Pineider, P. Sainctavit, C. Danieli, E. Otero, C. Sciancalepore, A. M. Talarico, M.-A. Arrio, A. Cornia, D. Gatteschi, R. Sessoli, *Nat. Mater.* **2009**, *8*, 194 – 197; f) M. Ganzhorn, S. Klyatskaya, M. Ruben, W. Wernsdorfer, *Nat. Nanotechnol.* **2013**, *8*, 165 – 169.

[2] R. Sessoli, D. Gatteschi, A. Caneschi, M. A. Novak, *Nature* **1993**, *365*, 141 – 143.

[3] a) S. Osa, T. Kido, N. Matsumoto, N. Re, A. Pochaba, J. Mrozinski, *J. Am. Chem. Soc.* **2004**, *126*, 420 – 421; b) N. Ishikawa, M. Sugita, T. Ishikawa, S.-y. Koshihara, Y. Kaizu, *J. Am. Chem. Soc.* **2003**, *125*, 8694 – 8695; c) D. N. Woodruff, R. E. P. Winpenny, R. A. Layfield, *Chem. Rev.* **2013**, *113*, 5110 – 5148; d) R. J. Blagg, L. Ungur, F. Tuna, J. Speak, P. Comar, D. Collison, W. Wernsdorfer, E. J. L. McInnes, L. F. Chibotaru, R. E. P. Winpenny, *Nat. Chem.* **2013**, *5*, 673 – 678; e) S.-D. Jiang, B.-W. Wang, H.-L. Sun, Z.-M. Wang, S. Gao, *J. Am. Chem. Soc.* **2011**, *133*, 4730 – 4733; f) S. K. Langley, D. P. Wielechowski, V. Vieru, N. F. Chilton, B. Moubaraki, B. F. Abrahams, L. F. Chibotaru, K. S. Murray, *Angew. Chem. Int. Ed.* **2013**, *52*, 12014 – 12019; *Angew. Chem.* **2013**, *125*, 12236 – 12241.

[4] a) J. D. Rinehart, M. Fang, W. J. Evans, J. R. Long, *Nat. Chem.* **2011**, *3*, 538 – 542; b) J. D. Rinehart, M. Fang, W. J. Evans, J. R. Long, *J. Am. Chem. Soc.* **2011**, *133*, 14236 – 14239; c) S. Demir, J. M. Zadrozny, M. Nippe, J. R. Long, *J. Am. Chem. Soc.* **2012**, *134*, 18546 – 18549.

[5] a) J. M. Zadrozny, D. J. Xiao, M. Atanasov, G. J. Long, F. Grandjean, F. Neese, J. R. Long, *Nat. Chem.* **2013**, *5*, 577 – 581; b) J. M. Zadrozny, J. R. Long, *J. Am. Chem. Soc.* **2011**, *133*, 20732 – 20734; c) R. C. Poulten, M. J. Page, A. G. Algarra, J. J. Le Roy, I. López, E. Carter, A. Llobet, S. A. Macgregor, M. F. Mahon, D. M. Murphy, M. Murugesu, M. K. Whittlesey, *J. Am. Chem. Soc.* **2013**, *135*, 13640 – 13643; d) R. Westerström, J. Dreiser, C. Piamonteze, M. Muntwiler, S. Weyeneth, H. Brune, S. Rusponi, F. Nolting, A. Popov, S. Yang, L. Dunsch, T. Greber, *J. Am. Chem. Soc.* **2012**, *134*, 9840 – 9843; e) S.-D. Jiang, B.-W. Wang, G. Su, Z.-M. Wang, S. Gao, *Angew. Chem. Int. Ed.* **2010**, *49*, 7448 – 7451; *Angew. Chem.* **2010**, *122*, 7610 – 7613; f) N. F. Chilton, S. K. Langley, B. Moubaraki, A. Soncini, S. R. Batten, K. S. Murray, *Chem. Sci.* **2013**, *4*, 1719 – 1730.

[6] C. Görller-Walrand, K. Binnemans in *Handbook on the Physics and Chemistry of Rare Earths, Volume 23* (Eds.: Karl A. Gschneidner Jr., L. Eyring), North – Holland, Amsterdam, **1996**, pp. 121 – 283.

[7] M. A. AlDamen, J. M. Clemente-Juan, E. Coronado, C. Martí-Gastaldo, A. Gaita-Ariño, *J. Am. Chem. Soc.* **2008**, *130*, 8874 – 8875.

[8] a) K. R. Meihaus, J. R. Long, *J. Am. Chem. Soc.* **2013**, *135*, 17952 – 17957; b) L. Ungur, J. J. Le Roy, I. Korobkov, M. Murugesu, L. F. Chibotaru, *Angew. Chem. Int. Ed.* **2014**, *53*, 4413 – 4417; *Angew. Chem.* **2014**, *126*, 4502 – 4506.

[9] a) J.-L. Liu, Y.-C. Chen, Y.-Z. Zheng, W.-Q. Lin, L. Ungur, W. Wernsdorfer, L. F. Chibotaru, M.-L. Tong, *Chem. Sci.* **2013**, *4*, 3310 – 3316; b) J.-L. Liu, J.-Y. Wu, Y.-C. Chen, V. Mereacre, A. K. Powell, L. Ungur, L. F. Chibotaru, X.-M. Chen, M.-L. Tong, *Angew. Chem. Int. Ed.* **2014**, *53*, 12966 – 12970; *Angew. Chem.* **2014**, *126*, 13180 – 13184; c) Y.-C. Chen, J.-L. Liu, L. Ungur, J. Liu, Q.-W. Li, L.-F. Wang, Z.-P. Ni, L. F. Chibotaru, X.-M. Chen, M.-L. Tong, *J. Am. Chem. Soc.* **2016**, *138*, 2829 – 2837; d) J. Liu, Y.-C. Chen, J.-L. Liu, V. Vieru, L. Ungur, J.-H. Jia, L. F. Chibotaru, Y. Lan, W. Wernsdorfer, S. Gao, X.-M. Chen, M.-L. Tong, *J. Am. Chem. Soc.* **2016**, *138*, 5441 – 5450.

[10] a) S. Cardona-Serra, J. M. Clemente-Juan, E. Coronado, A. Gaita-Ariño, A. Camón, M. Evangelisti, F. Luis, M. J. Martínez-Pérez, J. Sesé, *J. Am. Chem. Soc.* **2012**, *134*, 14982 – 14990; b) S. K. Gupta, T. Rajeshkumar, G. Rajaraman, R. Murugavel, *Chem. Sci.* **2016**, *7*, 5181 – 5191; c) Y.-S. Ding, N. F. Chilton, R. E. P. Winpenny, Y.-Z. Zheng, *Angew. Chem. Int. Ed.* **2016**, *55*, 16071 – 16074; *Angew. Chem.* **2016**, *128*, 16305 – 16308.

[11] M. Gregson, N. F. Chilton, A.-M. Ariciu, F. Tuna, I. F. Crowe, W. Lewis, A. J. Blake, D. Collison, E. J. L. McInnes, R. E. P. Winpenny, S. T. Liddle, *Chem. Sci.* **2016**, *7*, 155 – 165.

[12] Y. Bi, C. Chen, Y.-F. Zhao, Y.-Q. Zhang, S.-D. Jiang, B.-W. Wang, J.-B. Han, J.-L. Sun, Z.-Q. Bian, Z.-M. Wang, S. Gao, *Chem. Sci.* **2016**, *7*, 5020 – 5031.

[13] a) L. Ungur, M. Thewissen, J.-P. Costes, W. Wernsdorfer, L. F. Chibotaru, *Inorg. Chem.* **2013**, *52*, 6328 – 6337; b) L. Ungur, L. F. Chibotaru, *Phys. Chem. Chem. Phys.* **2011**, *13*, 20086 – 20090; c) T. Shiozaki, W. Győrffy, P. Celani, H.-J. Werner, *J. Chem. Phys.* **2011**, *135*, 081106.

[14] L. Ungur, L. F. Chibotaru, *Chem. Eur. J.* **2016**. DOI: 10.1002/chem.201605102.

[15] G. Sheldrick, *Acta Crystallogr. Sect. A* **2008**, *64*, 112 – 122.

[16] W. Wernsdorfer, *Supercond. Sci. Technol.* **2009**, *22*, 064013.

Manuscript received: December 27, 2016
Accepted Article published: January 30, 2017
Final Article published: February 20, 2017